JOURNAL OF COMPUTATIONAL PHYSICS **125,** 425–433 (1996)
ARTICLE NO. 0104

Numerical Study of Three-Dimensional Flows Using Unfactored Upwind-Relaxation Sweeping Algorithm

G.-C. ZHA* AND E. BILGEN

Department of Mechanical Engineering, Ecole Polytechnique, University of Montreal, P.O. Box 6079, St. A, Montreal, Quebec, Canada H3C 3A7

Received December 10, 1993; revised May 30, 1995

The linear stability analysis of the unfactored upwind relaxation-sweeping (URS) algorithm for 3D flow field calculations has been carried out and it is shown that the URS algorithm is unconditionally stable. The algorithm is independent of the global sweeping direction selection. However, choosing the direction with relatively low variable gradient as the global sweeping direction results in a higher degree of stability. Three-dimensional compressible Euler equations are solved by using the implicit URS algorithm to study internal flows of a non-axisymmetric nozzle with a circular-to-rectangular transition duct and complex shock wave structures for a 3D channel flow. The efficiency and robustness of the URS algorithm has been demonstrated.

INTRODUCTION

To obtain high efficiencies for steady state 3D flow simulations, implicit algorithms are preferred for their larger time step allowed. The Beam–Warming [1] or Briley–McDonald's [2] approximation factorization ADI scheme has made initially the most important contributions to the implicit algorithm development in the mid-1970s and has been a successful method, particularly for 2D cases. For three-dimensional hyperbolic cases, however, the algorithm employing spacial central discretization appears to be only conditionally stable [3]. With the appearance of the characteristic-based upwind schemes in the 1980s, the two-factor scheme based on a lower–upper (LU) factorization proposed by Steger and Warming [4] and Jameson and Turkel [3] became popular as an alternative to the ADI method to solve 3D flow fields. Even though the LU factorization method is stable, the time step is still limited due to the factorization error. Rai and Chakravarthy [5] suggested a Newton subiteration technique to drive the factorization error to zero at each time step, which makes the LU factorization methods have larger time steps than the noniterative schemes. This idea was successfully applied to 3D viscous flow fields by Simpson and Whitfield [6]. However, the iterative approach needs additional computation which is offset to some extent by larger time step sizes. Edwards and McRae [7] developed their nonlinear relaxation solver for 3D viscous flows with the mixture of upwind and central differencing. The method is shown to be efficient, but still related to the LU factorization.

Employing the upwind schemes in 2D cases, implicit unfactored relaxation algorithms demonstrate their striking convergency rate due to large time steps allowed [8–11]. For 3D cases, the achievements, however, are not so impressive. Candler and MacCormack [12] extended MacCormack's 1984 implicit unfactored algorithm to 3D and solved hypersonic flow fields using the Gauss–Seidel line relaxation with alternating sweeps. MacCormack modified the algorithm by implementing block tridiagonal inversions in two directions with Gauss–Seidel relaxation in the third direction to improve the robustness [13]. The rapid convergency rate has been obtained by both the algorithms. One disadvantage for these algorithms is the large computational work per time step, not because of the vectorization difficulty, which is shown to be achievable by McMaster *et al.* [14], but mainly because the Gauss–Seidel iteration for the fully implicit discretization usually needs more than one sweep, often two, in the sweeping direction. It is noted that two sweeps for sub- or transonic flows in the global field with one or two block tridiagonal matrix inversions at the local planes are usually CPU time intensive. A different unfactored 3D algorithm is developed by Paoletti *et al.* [15] using the conjugate gradient squared (CGS) iterative algorithm with ADI as a preconditioner. The algorithm is therefore called CGS-ADI. It uses the spatial central differencing and the artificial dissipation has to be added. An efficient ADI preconditioner is necessary for CGS-ADI. Otherwise a large number of CGS iterations may be required for each time step and it would offset the advantages of a large time step. More efforts are needed to develop robust unfactored 3D algorithms for they have theoretically the potential to obtain a rapid convergency rate and to save CPU time.

In 1990, Zha and Liu [16] suggested an unfactored upwind relaxation-sweeping (URS) algorithm. The URS method solves the 3D Euler equations by using a Gauss–

* Current address: Dept. of Mechanical and Aerospace Engineering, Rutgers, The State University of New Jersey, Piscataway, NJ, 08855-0909.

0021-9991/96 $18.00

Seidel-like iterative method. In this method, large time steps can be used and memory requirements are modest. In addition, it only requires one sweep in the global field and therefore the CPU time per time step is saved. In the cited reference, although the basic idea was described, detailed computational tests and stability analysis were not presented. The algorithm was successfully extended to solve 3D Navier–Stokes equations with a CFL number up to more than a million [17]. But the previous applications [16, 17] were mainly for simple geometries with simple physical phenomena. In these studies, Van Leer's flux-vector splitting (FVS) technique was used for its good representation of inviscid flow fields and efficiency [9–11, 18], although other upwind schemes could also be used including the one suggested by Zha and Bilgen [20].

The aim of this study is to solve more complex 3D problems using the URS algorithm with the Euler equations, to present a linear stability analysis, and to demonstrate the efficiency and robustness of the algorithm. The computational cases chosen are all internal flows involving mainly transonic duct flows due to the current interest in nonaxisymmetric exhaust nozzles.

GOVERNING EQUATIONS

The nondimensional form of the three-dimensional Euler equations in conservation law form and in Cartesian coordinates is

$$\frac{\partial U}{\partial t}+\frac{\partial F}{\partial x}+\frac{\partial G}{\partial y}+\frac{\partial H}{\partial z}=0, \tag{1}$$

where

$$U=\begin{bmatrix}\rho\\ \rho u\\ \rho v\\ \rho w\\ e\end{bmatrix},\quad F=\begin{bmatrix}\rho u\\ p+\rho u^2\\ \rho uv\\ \rho uw\\ (e+p)u\end{bmatrix},\quad G=\begin{bmatrix}\rho v\\ \rho uv\\ p+\rho v^2\\ \rho vw\\ (e+p)v\end{bmatrix},$$

$$H=\begin{bmatrix}\rho w\\ \rho uw\\ \rho vw\\ p+\rho w^2\\ (e+p)w\end{bmatrix}.$$

The pressure p is determined by the ideal-gas law,

$$\mathbf{p}=(\boldsymbol{\gamma}-\mathbf{1})[\mathbf{e}-\boldsymbol{\rho}(\mathbf{u}^2+\mathbf{v}^2+\mathbf{w}^2)/\mathbf{2}], \tag{2}$$

where γ is the ratio of specific heats, taken as $\gamma = 1.4$; u, v, w are the velocities, and e is the total energy per unit volume.

Let

$$P=F\cdot i_x+G\cdot i_y+H\cdot i_z. \tag{3}$$

Using the Gauss theorem, the integral form of Eq. (1) is

$$\int_Q \frac{\partial U}{\partial t}\,dQ+\int_S P\cdot n\,dS=0, \tag{4}$$

where Q is the volume bounded by the surface S and $\mathbf{n}$ is the outward pointing unit vector normal to the surface. The equations are discretized in the physical domain on the arbitrary body-fitted grid by using the finite volume method.

UPWIND RELAXATION-SWEEPING (URS) PROCEDURE

The concept of upwind relaxation-sweeping is to select a direction with relatively small variable gradients as the global sweeping direction and to implement the local relaxation iteration on the block in the main flow direction [16]. The flow field is calculated by a series of global alternating outward/inward sweeps in the sweeping direction with the local forward/backward Gauss–Seidel iteration on each streamwise plane, one global sweep per time step. The global sweeping is also the time marching procedure.

The interface flux is evaluated using Van Leer's flux vector splitting:

$$P=P^{+}+P^{-}. \tag{5}$$

The detailed formulations are given in Ref. [16]. The MUSCL-type differencing is used [11]. Assuming the global sweeping in z-direction with increasing index k, Eq. (4) is implicitly discretized as

$$\begin{aligned}&\frac{U_{i,j,k}^{n+1}-U_{i,j,k}^{n}}{\Delta t}Q_{i,j,k}+P_{i+1/2,j,k}^{+n+1}+P_{i+1/2,j,k}^{-n+1})\cdot S_{i+1/2}\\ &+(P_{i-1/2,j,k}^{+n+1}+P_{i-1/2,j,k}^{-n+1})\cdot S_{i-1/2}\\ &+(P_{i,j+1/2,k}^{+n+1}+P_{i,j+1/2,k}^{-n+1})\cdot S_{j+1/2}\\ &+(P_{i,j-1/2,k}^{+n+1}+P_{i,j-1/2,k}^{-n+1})\cdot S_{j-1/2}\\ &+(P_{i,j,k+1/2}^{+n+1}+P_{i,j,k+1/2}^{-n})\cdot S_{k+1/2}\\ &+(P_{i,j,k-1/2}^{+n+1}+P_{i,j,k-1/2}^{-n+1})\cdot S_{k-1/2}=0.\end{aligned} \tag{6}$$

It is noted that there is one term, $P_{i,j,k+1/2,}^{-n}$, discretized explicitly. To make the solution independent of the time

step size, the implicit terms should be changed to delta form. To construct the implicit operator for the Gauss–Seidel iteration, the delta form is only implemented for the terms with the same k index. One implicit term left is moved to the RHS. Equation (6) is then changed to

$$\left[\frac{I}{\Delta t}Q + \sum\left\{\left(\frac{dP^+}{dU}\right)_k + \left(\frac{dP^-}{dU}\right)_k\right\}\right]\delta U^{n+1} = \text{RHS}, \tag{7}$$

where $\delta U^{n+1} = U^{n+1} - U^n$, $\Delta t^n = t^{n+1} - t^n$, n is the iteration index, and

$$\begin{aligned}\text{RHS} = -\,[&(P^{+n}_{i+1/2,j,k} + P^{-n}_{i+1/2,j,k})\cdot S_{i+1/2}\\ &+ (P^{+n}_{i-1/2,j,k} + P^{-n}_{i-1/2,j,k})\cdot S_{i-1/2}\\ &+ (P^{+n}_{i,j+1/2,k} + P^{-n}_{i,j+1/2,k})\cdot S_{j+1/2}\\ &+ (P^{+n}_{i,j-1/2,k} + P^{-n}_{i,j-1/2,k})\cdot S_{j-1/2}\\ &+ (P^{+n}_{i,j,k+1/2} + P^{-n}_{i,j,k+1/2})\cdot S_{k+1/2}\\ &+ (P^{+n+1}_{i,j,k-1/2} + P^{-n}_{i,j,k-1/2})\cdot S_{k-1/2}].\end{aligned} \tag{8}$$

In matrix notation, Eq. (7) can be expressed as

$$M_k \delta U^{n+1}_k = \text{RHS}^{n,n+1}. \tag{9}$$

This equation represents the basic methodology of URS which, by using implicit–explicit hybrid discretization, inverts the implicit matrices locally at a block with the same index k and then sweeps globally block by block to solve the whole flow field. The RHS is evaluated by the variables at both time level n and $n + 1$.

The line Gauss–Seidel iteration is employed to invert the matrices at the local block k. To keep the diagonal dominance and save computational work, the first-order differencing is used for the implicit terms and, therefore, the matrix $\mathbf{M}_k$ is penta-diagonal. Two sweeps are implemented at the local block k, one forward and the other backward. Implementation of two sweep iterations is an approximation. An inner iterative approach such as that suggested by Taylor *et al.* [21] to drive down the error at the local block to a tolerable value may allow larger time steps. Such an inner iteration approach is, however, not employed in this paper. After two local sweeps, the global iteration proceeds to the next block. In this paper, the global sweeping starts with the inner solid wall with a increasing k index. The variables are updated at each block soon after the two local sweeps for the Gauss–Seidel iteration are completed. When the global iteration sweeps up to the outside solid wall, all the variables at time level $n + 1$ are obtained and then the sweeping direction is reversed with a decreasing k index to continue the iteration for the next time step. As shown in Eq. (8), the RHS is not evaluated completely by using the variables at time level n and contains one term, $P^{+n+1}_{i,j,k-1/2}$, which is available at the completion of the iteration at the $k - 1$ block. When the global iteration sweeps in the direction with the decreasing k index, the explicit term in Eq. (6) is $P^{+n}_{i,j,k-1/2}$, instead of $P^{-n}_{i,j,k+1/2}$; the implicit term at time level $n + 1$ in Eq. (8) is $P^{-n+1}_{ijk+1/2}$, instead of $P^{+n+1}_{ijk-1/2}$. The RHS of Eq. (8) is evaluated by using the third-order biased-upwind differencing. The accuracy of a converged solution is controlled by the RHS. Therefore the algorithm possesses a third-order accuracy for steady state flows.

The points of the URS algorithm that are different from the three-dimensional standard Gauss–Seidel (SGS) are:

(1) URS is an implicit–explicit hybrid, instead of fully implicit.

(2) The RHS of the URS algorithm is calculated using the variables at both time levels n and $n + 1$, instead of only at level n.

(3) All the unknowns in a time level are solved by one global sweep, instead of multiple sweeps.

Such a difference brings the following advantages:

(1) the Jacobians and δU^{n+1} are only stored at one block for the local Gauss–Seidel iteration. The storage requirement is therefore in the order of a two-dimensional case and is largely saved.

(2) one global sweep in a time level saves CPU time per time step.

In summary, the improvement of the URS algorithm is that it has the high stability and convergence rate of the unfactored Gauss–Seidel-type iterative methods while the memory requirement and CPU time per time step is less.

The disadvantage of the URS algorithm is that it is not fully conservative for a given time level because variables at time level n and $n + 1$ are used at the same time to evaluate the residual. Therefore, it may be inappropriate to use it for unsteady problems.

STABILITY ANALYSIS

A Von Neumann stability analysis is carried out for the linear scalar model convection equation:

$$U_t + uU_x + vU_y + wU_z = 0. \tag{10}$$

This equation can be rewritten using the split characteristic values with nonnegative and nonpositive signs as

$$U_t + (u^+ + u^-)U_x + (v^+ + v^-)U_y + (w^+ + w^-)U_z = 0, \tag{11}$$

where

$$u^+ = \frac{u+|u|}{2} \geq 0, \quad u^- = \frac{u-|u|}{2} \leq 0$$

$$v^+ = \frac{v+|v|}{2} \geq 0, \quad v^- = \frac{v-|v|}{2} \leq 0$$

$$w^+ = \frac{w+|w|}{2} \geq 0, \quad w^- = \frac{w-|w|}{2} \leq 0.$$

Suppose the global sweeping is in the direction with increasing k index. Using first-order upwind differencing to discretize the model equation, i.e., backward differencing for the positive characteristic values and forward differencing for the negative characteristic values, we obtain

$$\begin{aligned} U^{n+1}_{i,j,k}(1+\alpha^+ + \beta^+ + \gamma^+ - \alpha^- - \beta^- - \gamma^-) \\ + \alpha^- U^{n+1}_{i+1,j,k} - \alpha^+ U^{n+1}_{i-1,j,k} \\ + \beta^- U^{n+1}_{i,j+1,k} - \beta^+ U^{n-1}_{i,j-1,k} \\ - \gamma^+ U^{n+1}_{i,j,k-1} - U^n_{i,j,k} + \gamma^- U^n_{i,j,k+1} = 0, \end{aligned} \tag{12}$$

where

$$\alpha^+ = \frac{u^+\Delta t}{h} \geq 0, \quad \alpha^- = \frac{u^-\Delta t}{h} \leq 0$$

$$\beta^+ = \frac{v^+\Delta t}{k} \geq 0, \quad \beta^- = \frac{v^-\Delta t}{k} \leq 0$$

$$\gamma^+ = \frac{w^+\Delta t}{l} \geq 0, \quad \gamma^- = \frac{w^-\Delta t}{l} \leq 0;$$

h, k, and l are the grid intervals in the x, y, and z directions.

Obviously, we have

$$\begin{aligned} |1+\alpha^+ + \beta^+ + \gamma^+ - \alpha^- - \beta^- - \gamma^-| > \\ |\alpha^-| + |-\alpha^-| + |\beta^-| + |-\beta^+| + |-\gamma^+|. \end{aligned} \tag{13}$$

Thus Eq. (12) is diagonally dominant and satisfies the convergence conditions for the iterative method. It is noted that the diagonal dominance is stronger than the fully implicit scheme because the explicit term does not make any contribution to the off-diagonal elements. According to Lax's equivalence theorem [22], for the time marching problems, we also have to prove that the roundoff error of the URS algorithm satisfies the stability condition which is the necessary and sufficient condition for convergence.

Suppose the roundoff error function is $E(x, y, z, t)$ which can be expressed by a Fourier series. Since the model equation is linear, superposition can be used and we may examine the behaviour of a single term of the series. Consider a single term,

$$e(x, y, z, t) = Ae^{iax}e^{iby}e^{icz}, \tag{14}$$

where A is the amplitude of a single wave which is a function of time; a, b, and c are the wave numbers in the x, y, and z direction within 2π length. The error function satisfies the discretized model equation with the same form for U due to the linearity of the model equation. Substituting the single term, Eq. (14), into Eq. (12) and rearranging the terms, the amplification factor is obtained,

$$\begin{aligned} g &= \frac{A^{n+1}}{A^n} \\ &= (1-\gamma^- e^{i\varphi})/(1+\alpha^+ + \beta^+ + \gamma^+ - \alpha^- - \beta^- - \gamma^- \\ &\quad + \alpha^- e^{i\theta} \\ &\quad - \alpha^+ e^{-i\theta} + \beta^- e^{i\phi} - \beta^+ e^{-i\phi} - \gamma^+ e^{-i\varphi}), \end{aligned} \tag{15}$$

where $\theta = ah$, $\phi = bk$, $\varphi = cl$ are the differences of the wave phase angles of two neighbouring grid points in the x, y, and z directions.

From Eq. (15), we have

$$\begin{aligned} g^2 = [1 - 2\gamma^- \cos\varphi + (\gamma^-)^2]/\{[1 + (\alpha^+ - \alpha^-)(1-\cos\theta) \\ \times (\beta^+ + \beta^-)(1-\cos\phi) + \gamma^+(1-\cos\varphi) - \gamma^-]^2 \\ + [(\alpha^+ + \alpha^-)\sin\theta + (\beta^+ + \beta^-)\sin\phi + \gamma^+\sin\varphi]^2\} \end{aligned} \tag{16}$$

by taking the limits, with

$$\cos\theta = 1, \quad \cos\phi = 1, \quad \cos\varphi = 1$$

$$\sin\theta = 0, \quad \sin\phi = 0, \quad \sin\varphi = 0,$$

the numerator of Eq. (16) reaches the maximum and the denominator reaches the minimum. Therefore, the amplification factor reaches the maximum value:

$$g^2_{\max} = \frac{(1-\gamma^-)^2}{(1-\gamma^-)^2} = 1. \tag{17}$$

Thus we have

$$g^2 \leq g^2_{\max} = 1, |g| \leq 1. \tag{18}$$

Therefore, we conclude that, for the linear model equation, the URS algorithm with the first-order differencing is unconditionally stable. Equations (13) and (18) still apply when the global sweeping is in the direction of the decreasing k index due to the symmetry of the model equation. Therefore the stability is independent of the selection of the global sweeping direction.

It can be seen from Eq. (15) that, if $\gamma^- \to 0$, $\Delta t \to \infty$, the amplification factor

$|g_|| \to 0$. That is, the maximum dumping occurs when $\gamma^- \to 0$, $\Delta t \to \infty$. These conditions are weaker than the fully implicit unfactored scheme for which the maximum dumping occurs when $\Delta t \to \infty$. The extra condition, $\gamma^- \to 0$, is due to the explicitly discretized term.

$|\gamma^-|$ to be small means that the convection speed $|w^-|$ is small when a time step size and grid spacing are fixed. That is, even though the URS is unconditionally stable, if we choose the direction with the relatively low variable gradients as the global sweeping direction, the URS can result in a higher degree of stability. This is the theoretical base of the URS scheme.

It should be recalled that the above conclusions are all based on discretization using first-order differencing. In this paper, third-order differencing is employed for the evaluation of the RHS to obtain higher order accuracy solutions. The advantages of using a first-order differencing on the LHS are: (1) diagonal dominance of the coefficient matrix is retained and, therefore, the iteration convergency conditions are satisfied; (2) CPU time can be saved to solve the implicit operator since only the block tridiagonal matrixes need to be inversed. If a higher order differencing is used for the LHS, the diagonal dominance will be lost and, therefore, underrelaxation must be used. Block pentadiagonal matrixes must be solved for a higher order differencing and, therefore, more computational work is necessary. The disadvantage of the inconsistent differencing order for the LHS and the RHS is that the convergency rate will be reduced, compared with the consistent discretization.

RESULTS AND DISCUSSION

To validate the algorithm, three cases were calculated. Unless indicated, first-order differencing for the LHS and third-order differencing for the RHS were used. The convergence criterion used in this paper for all cases is that the maximum L2 norm of the RHS be reduced to machine zero.

Case 1 is a transition duct with a nonaxisymmetric transonic nozzle. The need for innovative jet-engine exhaust systems with multifunction capability is being met by various nonaxisymmetric nozzle concepts. A transition duct is needed to connect the axisymmetric engine to the nonaxisymmetric nozzle through a smooth progression of geometrically similar cross sections. Such a transition duct with a nonaxisymmetric transonic nozzle designed and tested by Burley *et al.* [23] are calculated. The characteristic geometric parameters for the transition duct are: L/D = 1.00, $\alpha_1 = 42.7°$, $\alpha_2 = 25.9°$, $A_{cs} = 20.1408$ in^2, where L/D is ratio of the transition duct length to the entrance diameter, α_1 is the maximum slope angle of transition along the sidewall, α_2 is the maximum slope angle of transition along the top or bottom walls, A_{cs} is the cross-sectional area. To

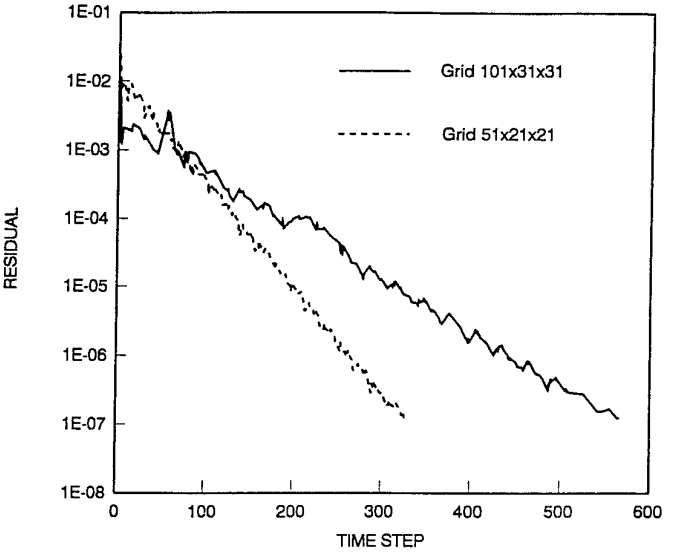

FIG. 1. The convergence histories of the calculation for the transition duct with the nozzle.

prevent cases with flow separation, α_1 and α_2 are chosen to be less than 45° as suggested by Stevens *et al.* [24]. Therefore with a little probability of separation, the Euler equations may predict well the general feature of the flow field. In the experimental study [23], the entrance flows with and without swirl were tested. The swirl flow is considered to be able to alleviate some flow separation by imparting a radial component to the velocity vectors. More importantly, they can be used to reduce the noise associated with the jet exhaust. In the experiment, the swirl flow was induced by installing 12 vanes with a 20° angle incline to the axis. Both flows with and without entrance swirl were calculated in this paper. To test the dependence of the convergence rate on the grid size, $51 \times 21 \times 21$ and $101 \times 31 \times 31$ grid sizes were calculated. The flow with entrance swirl is presented here, a case with a lower convergency rate. The maximum CFL number used is 500 for the grid $51 \times 21 \times 21$ and 540 for $101 \times 31 \times 31$. Single precision is used and the residuals are driven down to machine zero by using 320 iterations for the coarse grid and 581 iterations for the fine grid shown in Fig. 1. It is seen that the convergency rates are rapid. However, they depend on the grid size and are slower for the finer grid. The Mach number distribution along the center line is from subsonic to supersonic. Figure 2 presents the calculated pressure distributions along the side and bottom wall center lines, compared with the experiments with and without entrance swirl flow. The result with no swirl flow in Figs. 2a and b agrees very well with the experiment. The computational result almost goes through the experimental points. The pressure has a sharp rise at the throat due to the short compression right after the sonic line and goes

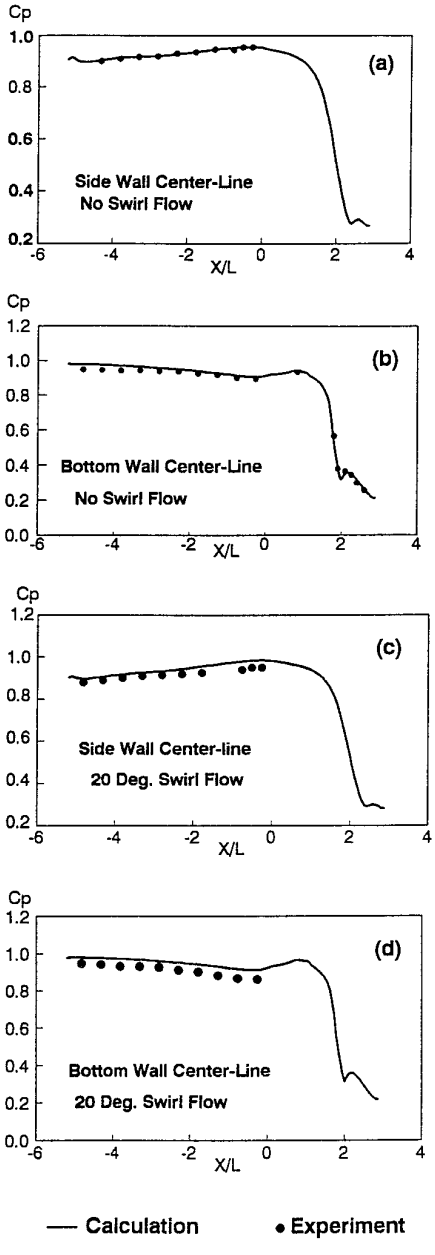

FIG. 2. Pressure distributions of the transition duct and the nozzle. Lines show the calculations and solid circles the experimental results.

down soon after the throat due to the supersonic acceleration. For the case with entrance swirl flow, experimental data are only avilable for the transition duct shown in Figs. 2c and d. It is seen that the pressure values are higher than the experimental data near the end of the transition duct. The main reason may be that it is not easy to simulate the entrance swirl flow accurately. We assumed that the entrance flow had a uniform swirl angle at the entrance plane. The experimental swirl device produces wakes behind the vanes and vane shaft and the flow entering the transition duct is not uniformly swirled. We also assumed that the swirl at the inlet of the duct is 20°. For the experiment, the swirl vanes have a distance from the duct inlet. The swirl flow may not be kept exactly at 20° when it approaches the inlet of the duct due to the influence of the wall boundary layers and the wakes. In fact, our computational experiments showed that the inlet boundary condition had quite a strong influence on the results. Despite such approximations, the computational result generally agrees well with the experiment as shown in Fig. 2 with the maximum error 3.6%.

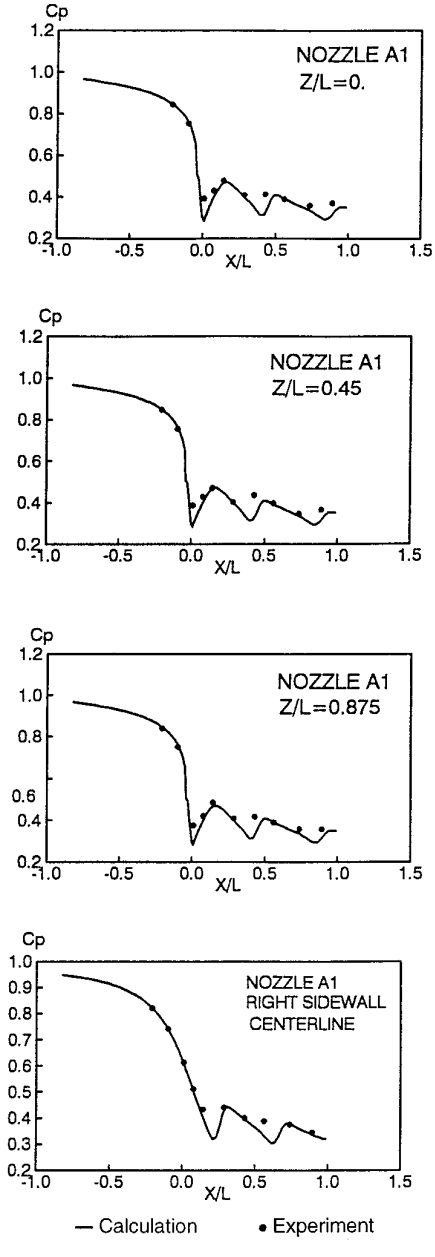

FIG. 3. Pressure distributions of the nozzle. Lines show the calculations and solid circles the experimental results.

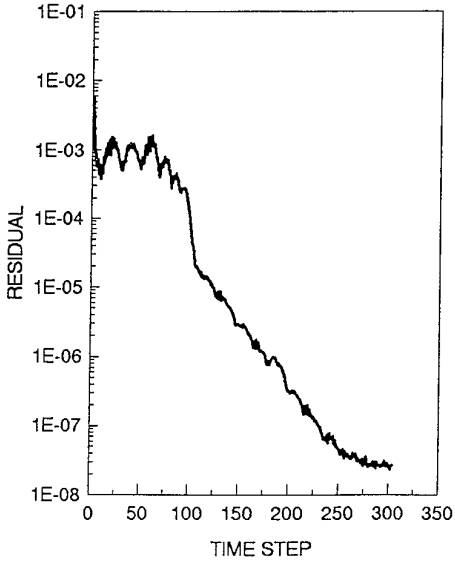

FIG. 4. The convergency history of the transonic nozzle.

It is interesting to investigate the transverse flow caused by the entrance swirl flow. When there is no entrance swirl, the cross flow is completely produced by the three-dimensional geometry and is symmetric with respect to two major axis planes. There is no vortex in the flow. When there is entrance swirl flow, the cross flow circulates in one direction induced by the swirl vanes. Such a flow picture retains for a short distance. With the flow going in and the cross section changing to elliptic, the circulation is split and is not symmetric anymore. There two points, one which is on the upper-right border and the other which is symmetrically on the lower left border, divide the transverse flow into two streams going to left and right. A vortex is kept around the center of the section. Such a cross flow field structure is maintained along the nozzle from the subsonic part to the supersonic part until the exit of the nozzle. The flow field near the horizontal axis plane has tangential velocity components and the velocity magnitudes are higher than those without entrance swirl. It is what the designers want to keep the flow attached on the side walls, which may have large divergence angles. This may be mainly attributed to the entrance swirl flow. The separation can alter the cooling film at some places and cause cooling problems. There is no shock wave in this flow although it is transonic.

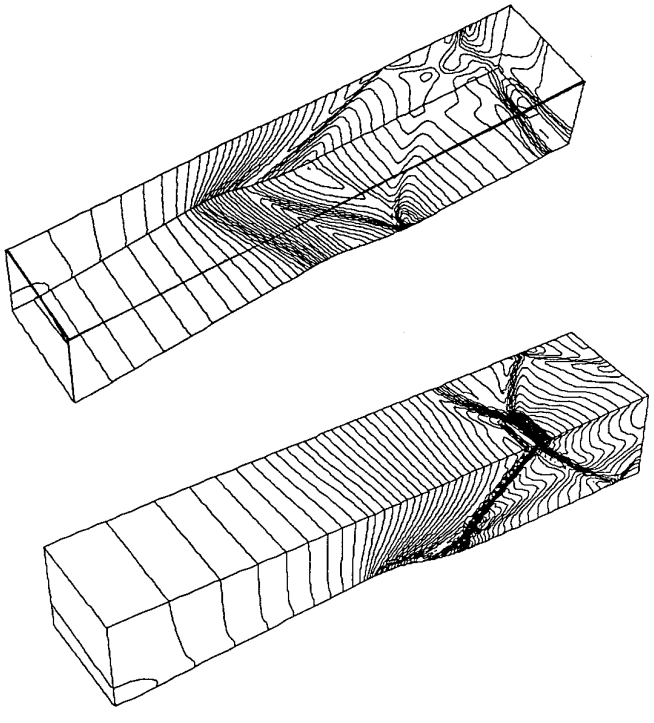

FIG. 5. The calculated Mach number contours of the channel on the wall; Pe/Pt = 0.545.

Case 2 is only a nonaxisymmetric transonic nozzle with no transition duct, which is chosen for a preliminary test of the flow with shock waves. The flow generally is two-dimensional because of the rectangular section. Oblique shock waves exist after the throat in both the computational and experimental flow fields. The shock waves are weak because the Mach number is only slightly greater than the one after the throat. The two shock waves extending from the lower and upper wall intersect at the center line of the nozzle and then reach the wall of the other side. After approaching the wall, the oblique shock waves reflect. These reflections intersect and reflect again until the flow approaches the exit of the nozzle. The intensity of the shock waves becomes weaker with repeated intersections and reflections. The pressure distributions in Fig. 3 show this phenomenon quantiatively at various locations. Figs. 3a, b, c are at the bottom wall with different locations from the center line (Z/L = 0.) to the one near the side wall (Z/L = 0.875). Figure 3d is the pressure distribution along the side wall center line. Most of the computational points agree very well with the experiment [25] within 2% deviation, except for the location at the first shock reflection. The computational shock reflection is not strong enough and the maximum error is there with the value up to 18%. Such a large deviation is believed to be because of the inviscid Euler solution which ignores the shock wave/turbulent boundary layer interaction. The maximum CFL number used for this case was 130. Figure 4 shows the convergency history which reaches machine zero rapidly.

Case 3 is a three-dimensional channel designed by Benay *et al.* [26] for an experimental study. In the experiment made at ONERA, this channel yielded a complex 3D flow field produced by the shock wave/boundary layer interaction. The Euler model used in this paper is not appropriate

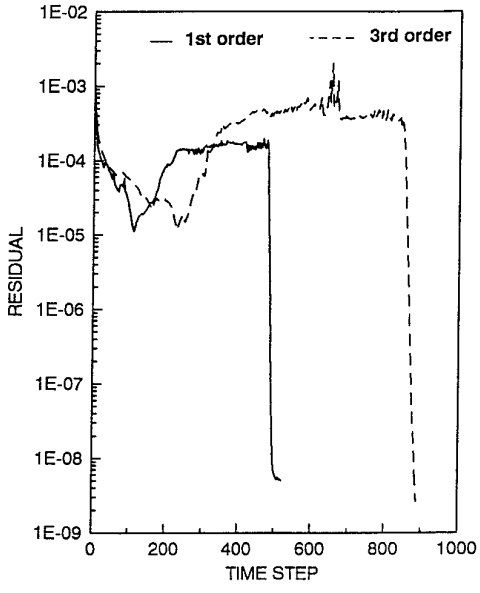

FIG. 6. Convergence histories of the 3D channel.

to capture the accurate physical solution. However, because of the complex shock wave structure, the computational convergence is usually difficult and the problem represents a good case to test the convergence behavior and robustness of the URS algorithm.

The channel has three flat walls and a humped lower wall. The upstream part of the hump is a ramp, inclined approximately at 7° from the horizontal. This ramp is followed by convex circular surfaces of 100 and 180 mm radius defined to ensure slope continuity everywhere. The angle formed by the hump crest and line and the channel axis equals 60°. The maximum height of the hump is 20 mm and the channel section is 120 mm wide and 100 mm high at the inlet. Figure 5 shows the Mach number contours on the walls corresponding to a dimensionless back pressure of 0.545, defined as the ratio of the back pressure to the total pressure. This value is take from Cambier and Escande [27] who solved the Reynolds averaged Navier–Stokes equations and obtained qualitative agreement with the experiment. The transverse shock location is not normal to the axis of the channel. Near the right side wall, the oblique shock is reflected on the upper wall and then on the bottom wall. Across the channel, two shock waves interact and a λ-shape shock wave forms. The upstream root of the shock has a weak reflection on he upper wall. The downstream root of the shock has quite strong reflections on both upper and left walls. The intensity of the shock wave becomes stronger near the right side wall. To study the convergency rate under the influence of the different order differencing used for the LHS and the RHS, both the first-order and the third-order differencing were tested for the RHS. Figure 6 shows the convergency histories. It is seen that the convergency rate with the first-order on the LHS and the third-order on the RHS is slower than with first-order differencing used on both sides. There are two reasons for this outcome. First, the inconsistent differencing order used for the LHS and the RHS will reduce the convergency rate, as mentioned in the section on stability analysis. Second, when the third order is used for the RHS, the numerical diffusion is less and the shock waves are sharper than those captured by using the first-order differencing. The crisp shock wave profiles make the convergence more difficult than by using the first-order differencing. The second reason for the slower convergency rate is considered to be more important. It is interesting to note from Fig. 6 that most of the iterations are in the high residual level and are used to form the shock waves. After overcoming the large residuals from the shock waves, they go down very sharply to machine zero and never go up again. The CFL number for this case is largely reduced, compared with the previous two cases. With the first-order differencing on the RHS, the maximum CFL number is 32, with the third-order on the RHS it is 24.

Even though the inviscid solution of case 3 has large quantitative deviation from the experimental results, the efficiency and robustness of the URS algorithm still has been demonstrated for this case.

CONCLUSIONS

The linear stability analysis shows that the unfactored upwind relaxation-sweeping algorithm is unconditionally stable. The algorithm is independent of the global sweeping direction selection. Further, by choosing the direction with relatively low variable gradient as the global sweeping direction, the algorithm can have a higher degree of stability. The three-dimensional compressible Euler equations are solved by the URS algorithm to study the internal flows of non-axisymmetric nozzles with a circular-to-rectangular transition duct. The cases with and without entrance swirl flow were calculated. The results agree well with the experiments. The computational experiments show that the URS algorithm is grid-size dependent. A 3D channel with complex shock wave structures also has been calculated. The results show that the URS algorithm is efficient and robust.

ACKNOWLEDGMENTS

The authors thank Mr. V. S. Pachanh and Mr. P. Leroux who have carried out geometrical calculations for the cases studied and also some of the computations. The scholarship from FCAR, Government of Quebec Province, to support the first author to do this work is acknowledged.

REFERENCES

1. R. Beam and R. F. Warming, *AIAA J.* **16,** 4 (1978).
2. W. R. Briley and H. McDonald, *J. Comput. Phys.* **24,** 4 (1977).

3. A. Jameson and E. Turkel, *Math. Comput.* **37,** 156 (1981).
4. J. L. Steger, and R. F. Warming, *J. Compu. Phys.* **40,** 2 (1981).
5. M. M. Rai, and S. R. Chakravarthy, *AIAA J.* **24,** 5 (1986).
6. L. B. Simpson, and D. L. Whitfield, *AIAA J.* **30,** 4 (1992).
7. J. R. Edwards and D. S. McRae *AIAA J.* **31,** 7 (1993).
8. R. W. MacCormack, AIAA *Paper 85-0032, Jan. 1985* (*unpublished*).
9. J. L. Thomas, B. Van Leer, and R. W. Walters, *AIAA J.* **28,** 6 (1990).
10. G. C. Zha, D. Z. Liu, and T. U. Ma, *Int. J. Numer. Methods Fluids* **9,** 5 (1989).
11. W. K. Anderson, J. L. Thomas, and B. Van Leer, *AIAA J.* **24,** 9 (1986).
12. G. V. Candler, and R. W. MacCormack, *AIAA Paper 87-0480, 1987* (*unpublished*).
13. R. W. MacCormack, AIAA *Paper 90-1520, June 1990* (*unpublished*).
14. D. L. McMaster, J. S. Shang, and D. Gaitonde, AIAA *89- 1948-CP, 1989* (*unpublished*).
15. S. Paoletti, M. Vitaletti, and P. Stow, AIAA *Paper 92-2668, 1992* (*unpublished*).
16. G. C. Zha, and D. Z. Liu, AIAA *Paper 90- 0129, 1990* (*unpublished*).
17. G. C. Zha, and E. Bilgen, AIAA 92-0023, 1992 (unpublished).
18. B. Van Leer, ''Flux-Vector Splitting for the Euler Equations,'' in *Lecture Note n Physics*, Vol. 170 (Springer-Verlag, New York/Berlin, 1982), p. 507.
19. M.-S. Liou, and C. J. Steffen, NASA TM 104404, May 1991 (unpublished).
20. G.-C. Zha, and E. Bilgen, *Int. J. Numer. Methods Fluids* **17** (1993).
21. A. C. Taylor III, W.-F. Ng, and R. W. Walters, *J. Compu. Phys.* **99** (1992).
22. R. D. Richtmyer, and K. W., Morton, *Difference Methods for Initial Value Problems*, 2nd ed., (Wiley Interscience, New York 1967).
23. J. R. Burley II, L. S. Bangert, and J. R. Carlson, NASA Technical Paper 2534, 1986 (unpublished).
24. H. L. Stevens, E. B. Thayer, and J. F. Fullerton, AIAA-81-1491, July 1981 (unpublished).
25. M. L. Mason, L. E. Putnam, and R. J. Re, NASA TP-1704, 1980 (unpublished).
26. R. Benay, J. Délery, and T. Pot, ONERA Rapport Technique no 70/7078 AN, 1986 (unpublished).
27. L. Cambier, and B. Escande, *AIAA J.* **11,** 11 (1990).